ISSN 0031-918X, The Physics of Metals and Metallography, 2015, Vol. 116, No. 10, pp. 1015–1028. © Pleiades Publishing, Ltd., 2015.
Original Russian Text © V.I. Ivashchenko, P.L. Skrynskii, O.S. Litvin, A.D. Pogrebnjak, V.N. Rogoz, G. Abadias, O.V. Sobol', A.P. Kuz'menko, 2015, published in Fizika Metallov i Metallovedenie, 2015, Vol. 116, No. 10, pp. 1069–1082.

STRUCTURE, PHASE TRANSFORMATIONS, AND DIFFUSION

Structure and Properties of Nanostructured NbN and Nb–Si–N Films Depending on the Conditions of Deposition: Experiment and Theory

V. I. Ivashchenko[a], P. L. Skrynskii[a], O. S. Litvin[b], A. D. Pogrebnjak[c], V. N. Rogoz[c], G. Abadias[d], O. V. Sobol'[e], and A. P. Kuz'menko[f]

[a] *Institute of Problems of Materials Science, National Academy of Sciences of Ukraine, ul. Krzhizhanovskogo 3, Kiev-142, 03680 Ukraine*

[b] *Institute of Physics of Semiconductors, National Academy of Sciences of Ukraine, pr. Nauki 41, Kiev, 03028 Ukraine*

[c] *Sumy State University, 40000 Sumy, ul. Rimskogo-Korsakova 2, Sumy, 40000 Ukraine*

[d] *Institut P, 14 allée Jean Monnet, 86073, Poitiers, France*

[e] *Kharkov Polytechnical Institute National Technical University, ul. Frunze 21, Kharkov, 61002 Ukraine*

[f] *Kursk State Technical University, Knowledge-Intensive Technologies Center of Collaborative Access, ul. 50 Let Oktyabrya 94, Kursk, 305040 Russia*

e-mail: v.rogoz2009 @gmail.com

Received July 18, 2014; in final form December 30, 2014

Abstract—The first results of studying the phase–structural state, properties, sizes of nanograins, hardness, and microstresses in nanocomposite NbN and Nb–Si–N films are given. The investigated films were obtained by the method of the magnetron sputtering of Nb and Si targets onto silicon substrates at different negative potentials at the substrate (from 0 to –70 V), nitrogen pressures P_N, and discharge powers at the targets. To determine the thermal stability of the films, they were annealed at 600, 800, and 1000°C in a vacuum. It was revealed for the first time that the NbN films have a two-phase nanocomposite structure, which consists of δ-NbN (NaCl structure type) and α'-NbN. The δ-NbN phase is also formed in Nb–Si–N films, where it is enveloped by an amorphous Si_3N_4 phase The hardness of the Nb–Si–N films reaches 46 GPa, which corresponds to the level of superhardness, while the hardness of the NbN nanocomposites is somewhat lower, but also very high (34 GPa). The experimental results for the Nb–Si–N films were explained based on the data obtained from the first-principles calculations of the NbN/Si_xN_y heterostructures by the molecular-dynamics method.

Keywords: NbN, Nb–Si–N, molecular dynamics, superhardness, nanocomposite

DOI: 10.1134/S0031918X15080062

1. INTRODUCTION

The nanostructured films are widely used for the surface hardening of cutting tools in connection with their high hardness, good corrosion resistance, and the low coefficient of friction [1]. Among quite numerous films, NbN-based coatings attract progressively greater attention. The hardness of these binary films is higher than that of the bulk NbN material (H_V = 14 GPa) and higher than the hardness of other binary nitride films (TiN, ZrN, VN). The hardness of the NbN films deposited under different conditions by the arc method reaches 34–49 GPa [2–7]. The NbN films were also obtained using magnetron sputtering (MS) [8–12], ion-beam deposition [13], using pulsed laser [14], etc. An increase in the hardness was achieved by the formation of a nanocomposite or a nanolayer structure based on niobium-nitride films [15–23]. Silicon nitrides are known to have a high thermal stability, low coefficient of friction, and high resistance to oxidation. Thus, it can be expected that the nanocomposite and multilayer Nb–Si–N structures will combine the properties of the component materials and will possess improved properties in comparison with the films of NbN.

Below, we consider films prepared by the method of magnetron sputtering. We examined recent studies concerning the deposition of NbN and Nb–Si–N films using this method. Some deposition parameters and the hardness of these films are given in Table 1.

It can be seen that, depending on the deposition parameters, NbN can form several different phases: δ-NbN (space group $Fm3m$), ε-NbN (space group $P\bar{6}m2$), and α'-NbN (space group $P6_3/mmc$). The formation of the hexagonal phase occurs at high values of the partial pressure of nitrogen and high bias voltage (U_s) at the substrate [8–10, 12]. The hardness of the hexag-

Table 1. Conditions of the deposition of Nb and Nb–Si–N films via magnetron sputtering and the mechanical properties of the films

Targets	Atmosphere	Measured parameters	NbN phase	Substrate	H, H_V, H_K, GPa	E, GPa	References
NbN film							
Nb	$Ar + N_2$	P_{N_2}, T_S	δ, α'	Silicon plate	$H = 25(\delta)$ $H = 38(\alpha')$	330(δ) 450(α')	[8]
Nb	$Ar + N_2$	P_{N_2}	δ, ε	Steel	$H = 30(\delta)$ $H = 45(\varepsilon)$	400(δ) 650(ε)	[9]
Nb	$Ar + N_2$	U_s	δ, α'	Silicon plate	$H = 38$	–	[10]
NbN	$Ar + N_2$	T_S, I_{NbN}, P_{N_2}	δ	Silicon plate	–	–	[11]
Nb	$Ar + N_2$	P_{N_2}, U_s	δ, α'	Steel	$H_K = 20.4$	–	[12]
Nb–Si–N films							
Nb	$Ar + N_2 + SiH_4$	P_{SiH_4}	δ	Stainless steel	$H_V = 53$	–	[15]
Nb, Si	$Ar + N_2$	I_{Si}	δ	Silicon plate	$H = 34$	330	[16–18]
Nb + Si	$Ar + N_2$	U_s	ε + δ	Silicon plate	$H_V = 29$	–	[19]
Nb + Si	$Ar + N_2$	P_{N_2}	ε + δ	Silicon plate	–	–	[20]

P_i is the partial pressure; T_s is the substrate temperature; I_i is the current supplied to the ith target; U_s is the bias voltage applied to the substrate; H, H_V, and H_K are the nanohardness, Vickers hardness, and Knoop hardness, respectively; and E is the elasticity modulus.

onal α' and ε phases of NbN is higher compared with cubic δ-NbN [8, 9].

However, it was revealed in [15] that the addition of silicon to 3.4 at % led to an increase in the hardness to 53 GPa. This increase in the hardness was connected with the formation of a nanocomposite structure of the Nb–Si–N films, which represented nanosized NbN grains built-in into the amorphous matrix of SiN_x [15–20]. An increase in hardness from 25 to 34 GPa was explained within the framework of the two-step mechanism due to the formation of a solid solution of the Si atoms in the NbN lattice and the formation of a nanocomposite material [16–18]. The hardness of the nanocomposite Nb–Si–N films reaches the maximum values of 30–34 GPa for 5–13 at % Si [17]. As in the case of NbN, the high bias voltages at the substrate and high partial pressure of nitrogen in the Nb–Si–N system favor the growth of ε-NbN grains [19, 20].

It can be seen from this brief analysis of the literature that, despite the previous studies of NbN and of Nb–Si–N films, no comparative study of these two types of films obtained at the identical parameters of deposition has yet not been conducted. Furthermore, the changes in the properties of such films depending on the voltage applied to the substrate were not studied either until now. It should be noted that no theoretical studies of these NbN/SiN_x nanostructures on the atomic level have been conducted, all the more so compared with the experiment.

Therefore, in this work, for the first time, we performed a complex study of NbN and Nb–Si–N films depending on the deposition conditions, in particular at different values of U_s. The films were investigated using the methods of atomic-force microscopy (AFM), X-ray diffraction (XRD), X-ray photoelectron spectroscopy (XPS), nanoindentation, and microindentation. The deposited nanocomposite films were annealed to determine their thermal stability. To interpret the experimental results obtained for the nanocomposite Nb–Si–N films, the first-principles calculations of NbN/Si_xN_y heterostructures have been performed in terms of the molecular-dynamics method.

2. EXPERIMENTAL AND CALCULATION PROCEDURES

The NbN-based films were applied to specular polished Si (100) plates by the dc magnetron sputtering of targets of Nb (∅72 × 4 mm, 99.999 at %) and Si (∅72 × 4 mm, 99.9 at %) in an atmosphere of argon and nitrogen at the following parameters of the deposition: the temperature of the substrate was T_s = 350°C; the bias voltage at the substrate was U_s = 0, –20, –40, –50, and –70 V; the flow rate (F) of argon F_{Ar} = 40 cm^3/s and of nitrogen F_{N2} = 13 cm^3/s; the pressure P_C = 0.17 Pa; the current at the Nb target I_{Nb} = 150 mA (P_{Nb} = 8.6 W/cm^2); and the current at the Si target I_{Si} = 100 mA (P_{Si} = 5.3 W/cm^2). The basic pressure in the vacuum chamber was better than 10^{-4} Pa. The distance between the targets and the holder of the substrate was equal to 8 cm. The dihedral

Table 2. Composition, designation, number of layers in the NbN film (N_L), and the change in the total energy $\Delta E_T = E_T(1400\ K) - E_T(0\ K)$ of the heterostructures under investigation

Initial heterostructure	Designation	Composition	N_L	ΔE_T, eV/atom
δ-NbN(001)/δ-Si_3N_4	δ-Si_3N_4(001)	$Nb_{40}N_{40}/Si_8N_8$	5	
ε-NbN(001)/ε-SiN	ε-SiN(001)	$Nb_{27}N_{27}/Si_9N_9$	6	0.000
ε-NbN(001)/Si_3N_4-like SiN	ε-Si_3N_4-SiN(001)	$Nb_{27}N_{27}/Si_9N_9$	6	0.017
ε-NbN(001)/Si_3N_4-like Si_2N_3	ε-Si_3N_4-Si_2N_3(001)	$Nb_{36}N_{36}/Si_6N_9$	8	0.000
δ-NbN(111)/δ-SiN	δ-SiN(111)	$Nb_{18}N_{18}/Si_9N_9$	4	0.000
δ-NbN(111)/Si_3N_4-like SiN	δ-Si_3N_4-SiN(111)	$Nb_{27}N_{27}/Si_9N_9$	6	–0.004
δ-NbN(111)/Si_3N_4-like Si_2N_3	δ-Si_3N_4-Si_2N_3(111)	$Nb_{45}N_{45}/Si_6N_9$	10	0.004

angle between the regions of the targets was ~45°. The silicon substrates were cleaned ultrasonically before they were placed into the vacuum chamber. In addition, the substrates were etched before the deposition in hydrogen plasma in a vacuum chamber for 5 min. The vacuum annealing of the coatings was carried out using a Pekly herrmann moritz JF1013 (France) setup equipped with a PFEIFFER HiCube 80 Eco (Germany) vacuum station at a pressure of the residual atmosphere $P_{ann} = 8 \times 10^{-4}$ Pa at the temperatures of 600, 800, and 1000°C for 1 and 2 h.

For investigating the elemental composition and morphology of the films, we used a JEOL-7001F-TTLS scanning electron microscope (SEM) equipped with an energy-dispersion X-ray (EDX) microanalyzer, a Lyncee Tec holographic microscope, and an OmegaScope confocal Raman spectroscope.

The crystal structure of the films was determined by X-ray diffraction (XRD) using a DRON-3M diffractometers and a Bruker Advanced 8 diffractometer in Cu$K\alpha$ radiation according to the Bragg–Brentano scheme. The average size of crystallites in the films was evaluated based on the broadening of peaks in the diffractograms according to the Scherrer formula. The binding energy of the elements in the films was determined with the aid of X-ray photoelectron spectroscopy (XPS, ES 2401, Soviet Union) in the spectrum of the Mg $K\alpha$ radiation ($E = 1253.6$ eV). As the standard, the peaks of Au $4f^{7/2}$ and Cu $2p^{3/2}$ with the binding energies of 84.0 ± 0.05 eV and 932.66 ± 0.05 eV, respectively, were used. The morphology of the surface was analyzed using a NanoScope Dimension 3000 (Digital Instruments, United States) atomic-force microscope. The hardness and elasticity modulus of the films were determined using a G200 nanoindenter with a trihedral Berkovich-type pyramid under loads in the range of 0.5–10 N. This range of loads was selected in order to obtain a noticeable plastic deformation of the film but avoid the influence of the material of the substrate. These nanohardnesses (H) and elasticity moduli (E) were determined from the load–displacement curves using the Oliver–Pharr method. The Knoop hardness (H_K) was estimated using a Micromet 2103 BUEHLER LTD Microhardness Tester under a load of 100 mN. The thickness of the films was determined using a Mikron-Gamma optical profilometer, as well as by studying SEM images of cross sections of samples with coatings.

2.1. Theoretical Methods

The NbN/Si_xN_y heterostructures consisting of one Si_xN_y interfacial monolayer between the layers of ε-NbN(001), δ-NbN(001), and δ-NbN(111) were simulated at 0 K and 1400 K using the first-principles molecular-dynamics (MD) method with subsequent static relaxation. We selected the configurations of the heterostructures that were most stable in the case of the TiN/Si_xN_y systems. The characteristics of the heterostructures investigated are given in Table 2.

The MD calculations were performed using the Quantum ESPRESSO-5.0.2 code [24] with periodic boundary conditions. The generalized gradient approximation (GGA) due to Perdew, Burke and Ernzerhof (PBE) [25] was used for the exchange–correlation energy and potential. For describing the electron–ion interaction, the ultrasoft pseudopotentials were used [26]. The criterion for the convergence for the total energy was taken equal to 1.36×10^{-5} eV. To accelerate the convergence, each eigenvalue was smeared by a Gaussian with a width $\sigma = 0.272$ eV. The initial heterostructures were improved, by the optimization of the basis vectors and the atomic arrangement inside the super-cell with the aid of the Broyden–Fletcher–Goldfarb–Shanno (BFGS) algorithm [27]. The MD calculations of the originally relaxed heterostructures were carried out at 1400 K with fixed parameters of the unit cell and fixed volume (NVT ensemble, constant number of particles–constant volume–constant temperature) for a time of 1.7 ps. The temperature of the system was kept constant via the recalculation of the speed, and the change

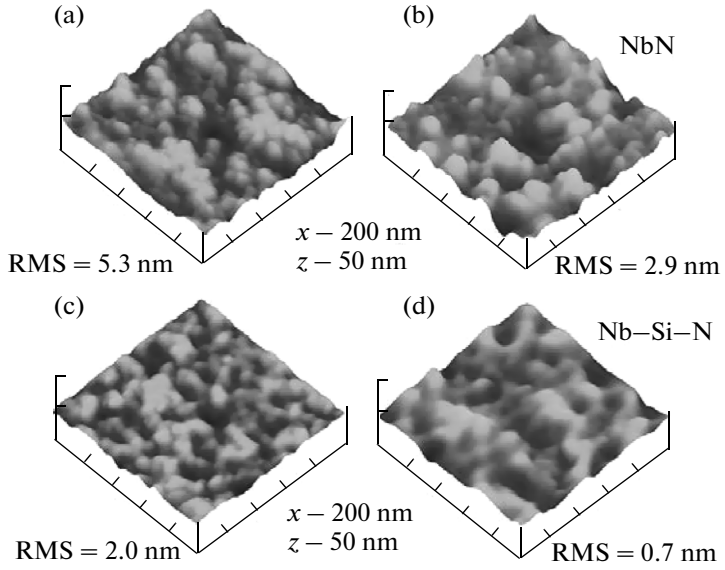

Fig. 1. AFM images of NbN films deposited at (a) $U_s = 0$ V (RMS = 5.3 nm) and (b) $U_s = -70$ V (RMS = 2.9 nm); and of Nb–Si–N films deposited at (c) $U_s = 0$ V (RMS = 2.0 nm) and (d) $U_s = -70$ V (RMS = 0.7 nm).

in the total energy was controlled at each time step of the MD procedure. All the structures reached an equilibrium state in a time of ~1 ps.

In the MD simulation, we used the cutting energy of 408 eV and one *k* point at the center of the Brillouin zone. The substantiation of this approach was confirmed in [28, 29].

After the MD balancing, the geometry of the heterostructures was optimized by the simultaneous relaxation of the basis vectors of the supercell and of the positions of atoms inside the supercell using the BFGS algorithm [27]. The Monkhorst–Pack (2 2 2) scheme [30] was used. The relaxation of the atomic coordinates and the supercell was considered terminated when the atomic forces were less than 25.7 MeV/Å, the stresses were less than 0.05 GPa, and the change in the total energy during the structural optimization of the iterative process was less than 1.36 meV. For the heterostructures, we introduced the abbreviations ZT and HT, which relate to the heterostructures obtained at 0 and 1400 K, respectively.

The tensile stress–strain curves were calculated according to the following scheme:

(1) we extended the supercell along the *c* axis with a small true deformation (~0.04);

(2) the basis vector **c** was fixed;

(3) the basis vectors **a** and **b** of the cell and atomic positions in the supercell were optimized simultaneously.

The cubic *B*1-type (*Fm*3*m*) structure of NbN was also studied for checking our computational method. The lattice parameter was calculated to be $a_{NbN} = 4.41$ Å, which is close to the experimental value 4.394 Å and it is comparable with other theoretical results (4.378–4.42 Å [31]).

3. RESULTS AND DISCUSSION

3.1. Experimental Results

Figure 1 shows the AFM topography of the surface of NbN and Nb–Si–N films deposited at different voltages applied to the substrate ($U_s = 0, -20, -40, -70$ V). It can be seen that the surface roughness decreases in the order NbN—Nb–Si–N, and with an increase in U_s. The smaller roughness of the surface of the Nb–Si–N films in comparison with NbN films can be connected with the presence of amorphous SiN_x, one of the components of the Nb–Si–N films (see below). Hence, it follows that an increase in the voltage U_s applied to the substrate during the deposition and the introduction of silicon favor the reduction of the surface roughness.

Figure 2 displays portions of the diffractograms of the coatings both without silicon and with silicon obtained at zero bias. It can be seen that upon the sputtering of niobium, there is formed the two-phase structure on the coating; along with the peaks from the cubic component (δ-NbN, NaCl-type structure, PDF no. 38-1155), strongly smeared peaks from the phase identified as α'-NbN (PDF no. 43-1420) are present. In the case of alloying with silicon (spectrum *2* in Fig. 2), peaks from the cubic δ-NbN phase are also revealed; however, in this case as the second system there are present diffraction peaks from the phase that we defined as Si_3N_4 (PDF no. 40-1129). One should also note the appearance of a preferred orientation of growth (200) for δ-NbN crystallites (both in the coatings with and without silicon).

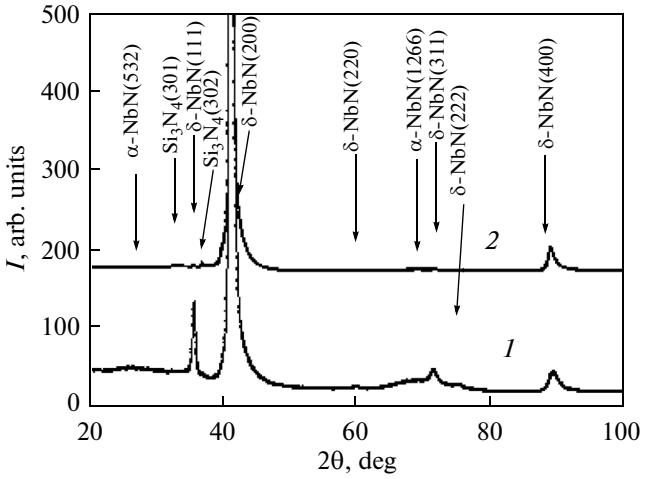

Fig. 2. Portions of diffractograms taken from (*1*) NbN and (*2*) Nb–Si–N films obtained without the application of a bias potential.

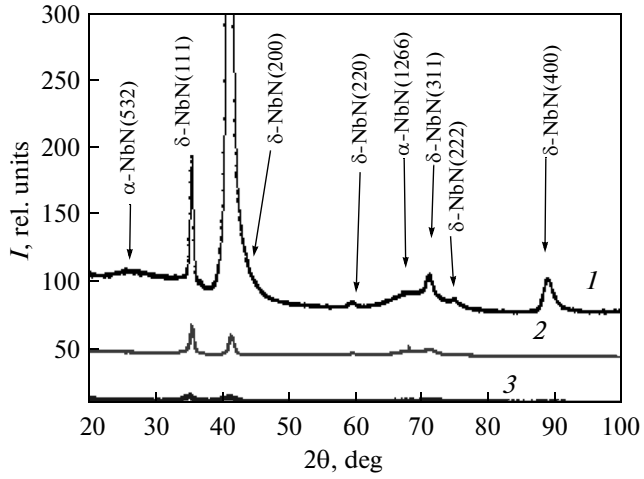

Fig. 3. Portions of diffractograms taken from niobium-nitride coatings obtained with the application of a negative bias potential: (*1*) $U_s = 0$ V, (*2*) $U_s = -40$V, (*3*) $U_s = -70$ V.

The analysis of substructural characteristics has shown that the coatings of the NbN system are strongly distorted. The level of microdeformations reaches 1.5%. The average size of the crystallites of the δ-NbN phase reaches 27 nm and, in the α'-NbN phase, it reaches ~3 nm. Coatings of the Nb–Si–N system are less distorted, and the microdeformation is about 0.5%. The average size of crystallites in this case is greater; it reaches 50 nm for crystallites of the δ-NbN phase and is close to 23 nm for the crystallites of the Si_3N_4 phase.

The asymmetry of the diffraction peaks from the δ-NbN phase on the side of larger angles indicates the presence of stacking faults, which usually appear under the action of the specific stress–strain state that arises during the formation of the coating.

For the Nb–N system, the application of a bias potential leads to the formation of crystallites of δ-NbN almost without a preferred orientation (Fig. 3). In the case of the Nb–Si–N film, the application of a bias potential determines a gradual decrease in the degree of texture up to the transition into a polycrystalline state without a preferred orientation of crystallites as the bias potential reaches –70 V (Fig. 4).

The calculation of substructure characteristics has shown that, in the Nb–N system, the sizes of the crystallites of the δ-NbN phase [32] in the presence of a negative bias potential during the deposition (–40 V) are 86 nm at a high value of microdeformations (2.1%). An increase in the negative bias to –70 V during deposition leads to a strong dispersion of the structure of the arising condensate (the average size of crystallites decreases to 17 nm). The value of the microdeformation in this case is 1.7%, which is somewhat lower than in the condensates formed while depositing at $U_s = -40$ V. The lattice parameter in the direction perpendicular to the film surface changes from 0.439 nm in the coatings obtained without applying the bias potential to 0.440 nm at $U_s = -70$ V.

In the Nb–Si–N system, the application of a negative bias potential of –20 V has led to a significant change in the average size of the crystallites of the δ-NbN phase and to the transition of the regions of the ordered Si_3N_4 phase into an amorphous-like state. The size of the crystallites of the δ-NbN phase decreased from 47 (at $U_s = -20$ V) to 27 (at $U_s = -40$ V) and even to 9.1 nm (at $U_s = -70$ V). The microdeformation of the crystallites in the entire range of the applied U_s remains at a level of 0.5%, rising to 0.6% at the greatest $U_s = -70$ V.

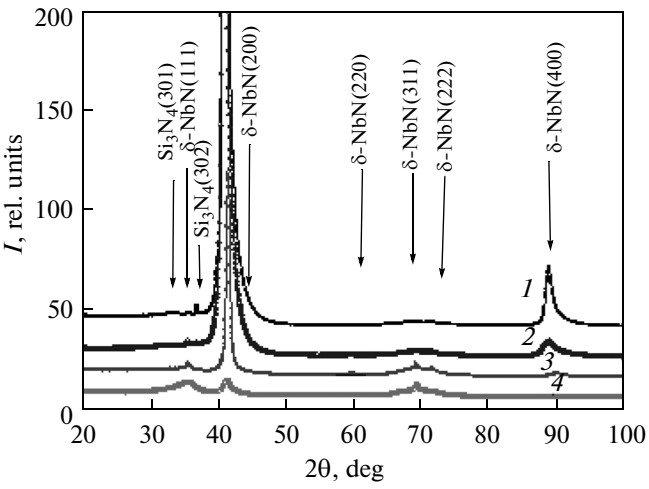

Fig. 4. Portions of diffractograms taken from the coatings of the Nb–Si–N system obtained with the application of a negative bias potential: (*1*) $U_s = 0$ V, (*2*) $U_s = -20$ V, (*3*) $U_s = -40$ V, and (*4*) $U_s = -70$ V.

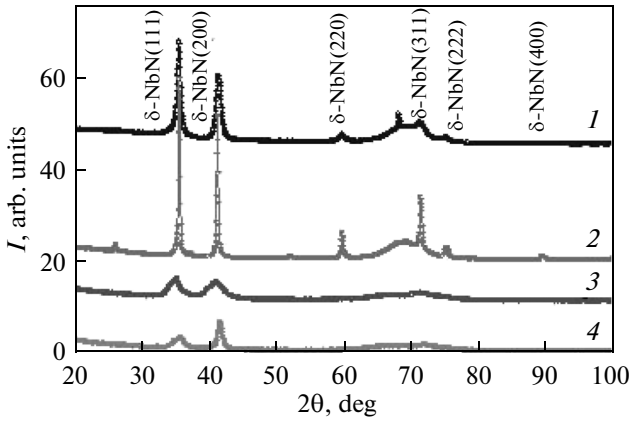

Fig. 5. Portions of diffractograms taken from niobium-nitride coatings obtained with the application of a negative bias potential: (*1*, *2*) –40 V and (*3*, *4*) –70 V; (*1*, *3*) prior to and (*2*, *4*) after annealing at 1000°C.

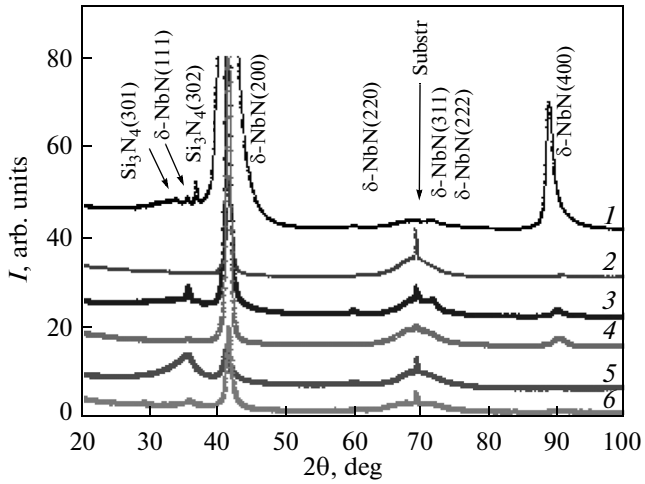

Fig. 6. Portions of diffractograms taken from coatings of the Nb–Si–N system obtained (*1*, *2*) without the application of a bias potential and with the application of a negative bias potential (*3*, *4*) –40 V and (*5*, *6*) –70 V; (*1*, *3*, *5*) prior to and (*2*, *4*, *6*) after annealing at 1000°C.

Figure 5 shows portions of diffractograms taken before and after the annealing of coatings of the NbN system at 1000°C. Note that annealing has led to a decrease in the lattice parameter of the δ-NbN phase: at $U_s = -40$ V, the decrease is from 0.439 to 0.437 nm after annealing with 1000°C and, at $U_s = -70$ V, the decrease is from 0.441 to 0.433 nm. This change is characteristic of the behavior of ion-plasma condensates upon the annealing and is determined by the relaxation of the initial (postcondensation) compressive stresses [38–41].

The analysis of the changes in the substructure characteristics upon the annealing has shown that, for the coatings obtained at $U_s = -40$ V, the annealing leads to an increase in the size of grains–crystallites to an average size of 200 nm and to a reduction in the microdeformations to 0.22%. In the case of the strong dispersity of the initial structure, the annealing at $U_s = -70$ V has led to an increase in the size of crystallites from 17 to 87 nm and to a significant decrease in the microdeformation (from 1.7 to 0.45%).

Figure 6 shows diffractograms for the of Nb–Si–N system after annealing at a temperature of 1000°C.

Note that, in the case of coatings of the Nb–Si–N composite, the annealing also leads to a decrease in the lattice parameter of the condensate. This is most strongly pronounced for the coatings deposited at $U_s = -70$ V, for which the lattice parameter of the δ-NbN phase decreased from 0.439 to 0.435 nm after a 2-h annealing at 1000°C (Fig. 6, spectra *5* and *6*).

The analysis of the substructure characteristics of this series of coatings has shown that the substructural state changes to the smallest degree upon the annealing of the samples obtained without the bias potential. The size of crystallites *D* changes from 50 to 67 nm, and the microdeformation changes from 0.5 to 0.47%.

As a result of the annealing, changes occur on the substructure level in the coatings obtained at $U_s = -40$ V. In this case, the annealing leads to an increase in *D* from 27 to 120 nm and to a significant relaxation of the distorted state (a decrease in microdeformation from 0.49% to 0.25%).

The annealing has influenced to a considerable extent the substructure characteristics of the films obtained at the greatest $U_s = -70$ V. After this annealing, the average size of crystallites increased from 9.1 to 150 nm, and the value of the microdeformation changed from 0.6 to 0.3%.

Not so significant changes that occur upon the annealing of the films obtained without the bias and at a small bias potential can be connected with the high concentration of silicon atoms in them, which exert a retarding effect. At the high bias potential, a strong change in the substructure characteristics upon the annealing can be caused by a considerably smaller influence of the silicon component because of its partial secondary sputtering from the growth surface during the deposition. To check this hypothesis, we performed a microprobe elemental analysis of the coatings obtained without the bias potential and at a high U_s (–70 V).

The results of the microprobe analysis of coatings of the Nb–Si–N system obtained without the bias potential and at $U_s = -70$ V are given in Table 3. It can be seen that, without the bias voltage, the Nb/Si ratio is equal to 2.57. The composition of the coatings obtained at $U_s = -70$ V is somewhat different; it can be seen that Nb/Si = 3.77. Thus, the application of a large negative bias potential led (as a result of the secondary sputtering) to a relative depletion of the light atoms from the coating, which was expected upon the discussion of the results of annealing.

A comparison of the results of the structural and elemental spectral analysis shows that at the high content of nitrogen there is formed a strong texture (200), whereas in the case of the ratio between nitrogen and other atoms that is close to 50 : 50 a polycrystalline structure is formed without a clearly pronounced preferred orientation of crystallites.

It should be noted that, in both cases, the content of Si in the coatings is somewhat overestimated, which is determined by the specific features of the method of the analysis of the silicon-containing coatings with a thickness to 2 μm on silicon substrates.

As can be seen from the appearance of the fracture of a coating (Fig. 7), its thickness is about 1.2 μm, and the dense (without cracks and pores) structure does not have a clearly pronounced columnar structure. This determines the good prospect of using these coatings as diffusion barriers.

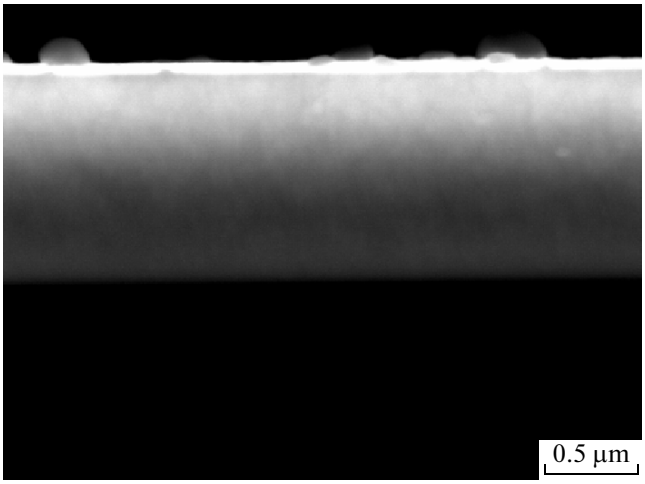

Fig. 7. Morphology of the fracture surface of coatings of the Nb–Si–N system deposited without the application of a bias potential.

Table 3. Results of the spectral analysys of the Nb–Si–N coatings obtained without a bias and with a bias potential −70 V

Element	Type of line (series)	Atomic concentration, % ($U_s = 0$ V)	Atomic concentration, % ($U_s = -70$ V)
N	*K*	61.25	50.28
Si	*K*	10.85	10.42
Nb	*L*	27.9	39.3

Figure 8a shows the surface of an NbN film obtained in the absence of a bias potential at the substrate. It can be seen that the film is of fairly good quality without pores; a globular structure is formed on the surface with globules sizes of approximately 100 nm. The ratio of the concentrations of Nb and N (Fig. 8c) is close to stoichiometric, i.e., $C_N = 51.79$ at % and $C_{Nb} = 48.21$ at %.

Figure 9a shows the image of the surface of an NbN/SiN_x coating obtained after the deposition with the application of a negative bias potential $U_s = -70$ V to the substrate. As can be seen from the results of the SEM and AFM analyses, the addition (introduction) of Si into NbN leads to a decrease in the roughness of the coating; at the same time, the microprobe analysis has shown that the concentration of Si is not very high and corresponds to approximately 4 at %. As is known from [15], this concentration of Si in the NbN/SiN_x system corresponds to the highest values of hardness, which can reach 53 GPa.

Figure 10 displays the dependence of the size of crystallites in the NbN and Nb–Si–N films on the

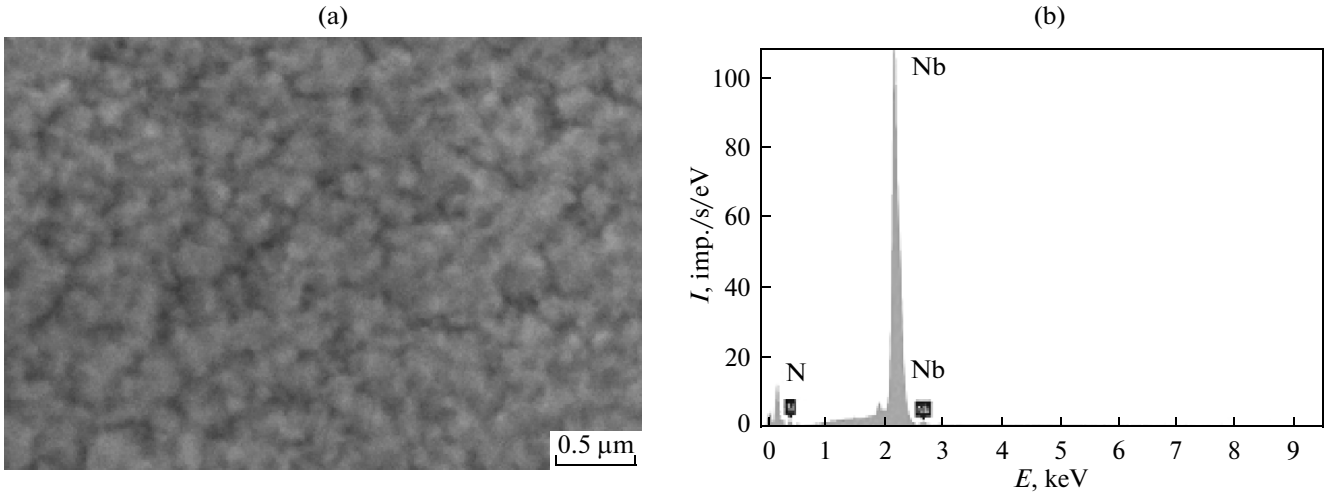

Fig. 8. (a) SEM image and (b) an EDX spectrum of an NbN coating obtained at $U_s = 0$ V.

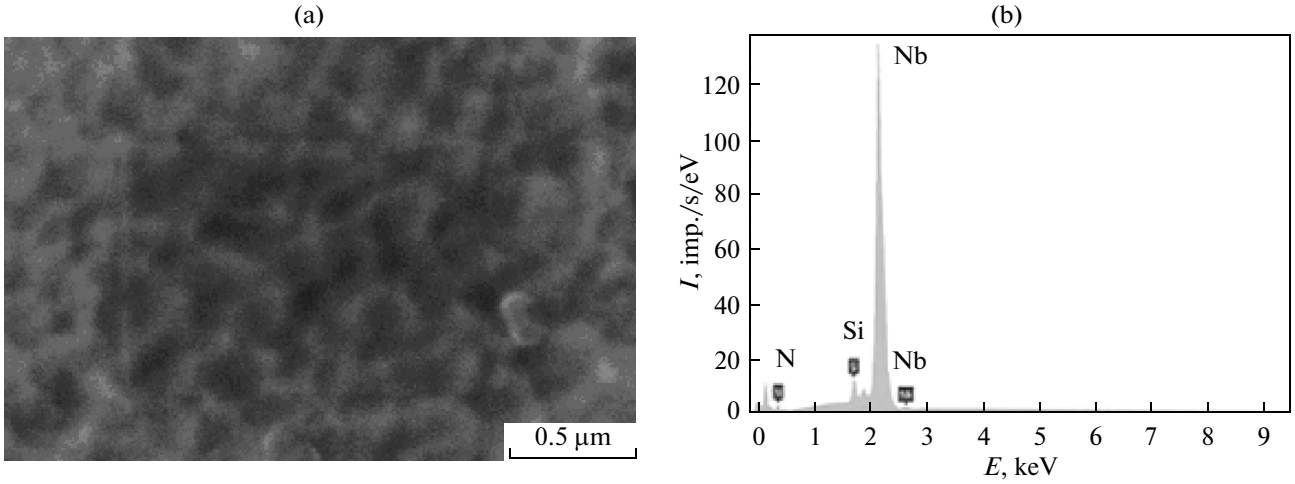

Fig. 9. (a) SEM image and (b) an EDX spectrum of an Nb–Si–N coating obtained at $U_s = -70$ V.

parameter U_s. The value of D decreases with an increase in U_s for Nb–Si–N and has an extremal dependence for NbN. After annealing, a substantial increase in the sizes of crystals is observed, which is connected with the processes of recrystallization, a decrease in the magnitude of microstresses, and a decrease in the amount of defects in the coating.

The results of the XPS studies for both the initial basic and annealed NbN and Nb–Si–N-films are represented in Fig. 11. It is known that, in the Nb compounds, upon annealing in contact with air, an oxide is formed [19], and the peaks at 204.07 eV and 206.88 eV can be identified as Nb 3*d* in NbN (203.97 eV [21]) and in $Nb_2N_{2-x}O_{3+x}$ (207.0 eV [33]). For the NbN films, the position of peak N 1*s* at 397.4 eV in the spectrum is defined by the Nb–N bonds, while for the Nb–Si–N films, this peak is located near 397.2 eV and can also be defined as N 1*s* in NbN (397.4 eV [19]). We assume that the asymmetry of the N 1*s* peak can be caused by Si–N bonds in Si_3N_4 (397.8 eV [34]).

Additional information about the bonds of Si in the Nb–Si–N-films comes from the XPS measurements of the Si 2*p* spectrum (Fig. 11). The peak with the

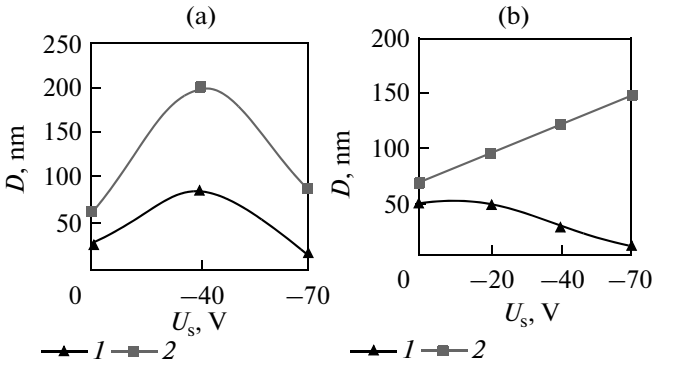

Fig. 10. Average size of crystallites (D) evaluated from the peak $\Theta \approx 41°$ (200) according to the Scherrer formula as a function of the bias voltage U_s at the substrate: (*1*) prior to and (*2*) after annealing: (a) NbN coating and (b) Nb–Si–N coating.

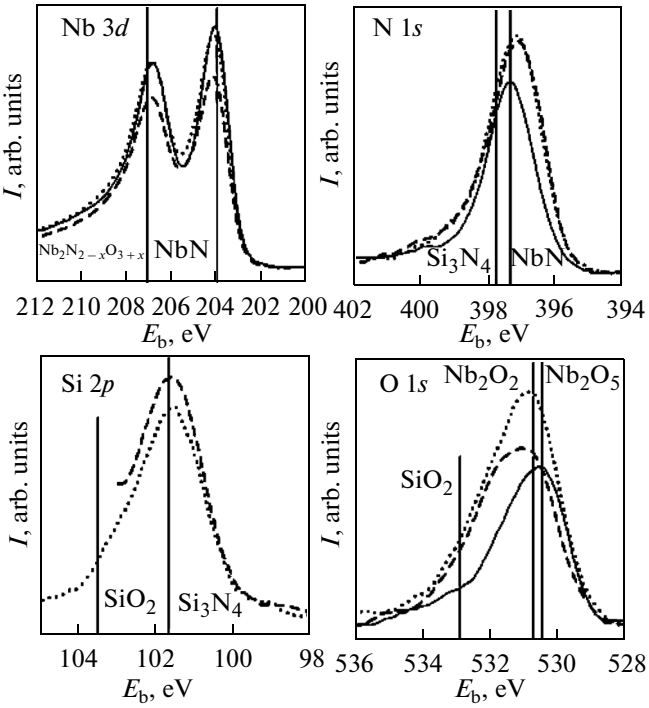

Fig. 11. XPS spectra of the energy levels in the initial NbN (solid line) and Nb–Si–N (dotted line) films, and in Nb–Si–N films annealed at 1000°C (dashed line). The vertical lines designate the binding energies of the XPS peaks: Nb 3*d* in NbN, 203.97 eV [21] and in $Nb_2N_{2-x}O_{3+x}$, 207.0 eV [33]; N 1*s* in NbN, 397.4 eV [19] and in Si_3N_4, 397.8 eV [34]; Si 2*p* in Si_3N_4, 101.7 eV and in SiO_2, 103.5 eV [34]; O 1*s* in Nb_2O_5, 530.4 eV, in Nb_2O_2, 530.7 eV, and in SiO_2, 532.9 [34].

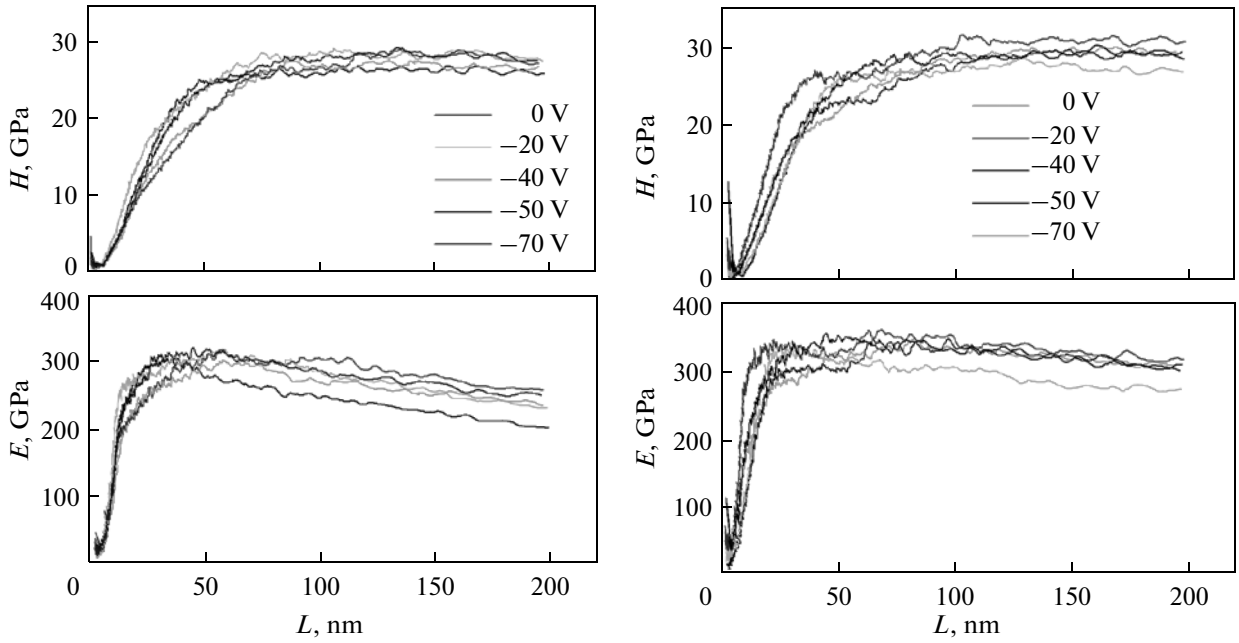

Fig. 12. Dependences of the nanohardness (H) and elasticity modulus (E) on the depth of penetration (L) of the nanoindenter for (a) NbN and (b) Nb–Si–N films deposited at different bias voltages $U_s = 0, -20, -40, -50$, and -70 V.

binding energy 101.7 eV belongs to Si in Si_3N_4 (101.7 eV in [34]), and the spread at 103.3 eV in the Si 2p spectrum of the annealed films occurs because of the effect of the Si–O bonds in SiO_2 (103.5 eV [34]). Finally, the O 1s spectra of the NbN and Nb–Si–N films are concentrated around 530.5 and 530.9 eV, respectively, and can be related to the Nb–O bonds in Nb_2O_5 (530.4 eV) and in Nb_2O_2 (530.7 eV [34]), respectively. In the case of Nb–Si–N-films, the Si–O bonds in SiO_2 can form a wide tail around 532.9 eV [34] (Fig. 11). Using the XPS data, we estimated the content of niobium, nitrogen, and silicon (C_{Nb}, C_N, and C_{Si}, respectively) in NbN and Nb–Si–N coatings. It was found that $C_{Nb} = 44.5$ at % and $C_N = 55.5$ at % for the NbN-films; and $C_{Nb} = 45.1$ at %, $C_N = 43.2$ at %, and $C_{Si} = 11.7$ at % for the Nb–Si–N-films, which coincides in order of magnitude with the results (EDX) of the microprobe analysis.

A comparison of the results presented in Figs. 1–11 makes it possible to establish the structure of the NbN and Nb–Si–N films. The NbN coatings are nanostructured films, and the Nb–Si–N-films have a nanocomposite structure, consisting of δ-NbN_x nanocrystallites embedded into the amorphous matrix of Si_3N_4 (nc-δ-NbN_x/a–Si_3N_4). In contrast to NbN coatings, the Nb–Si–N films reveal a preferred (200) orientation of grains. The films contain oxygen in the form of niobium oxides (after annealing at 600, 800, and 1000°C); the concentration of oxygen increases from a few percent to 20 at % at a temperature of 1000°C. We also assume that, in the case of the Nb–Si–N-coatings, oxygen is present in the form of SiO_2, which leads to its segregation along grain boundaries. Note that, despite the larger grain sizes, the roughness of the surface of Nb–Si–N-films is less than that of the NbN films. It can be assumed that the amorphous Si_3N_4 phase in the Nb–Si–N nanocomposite films can influence the relief of the surface [33–37]; for this reason, the roughness of the surface of nanocomposite films must be lower than that of NbN films.

The dependences of the nanohardness (H) and of the elasticity modulus (E) on the depth of penetration (L) of the indenter for the deposited films are represented in Fig. 12. It can be seen that, beginning with 75 nm, the nanohardness practically does not depend on the depth. The nanohardness and the elasticity modulus only weakly depend on U_s, increasing slightly with an increase in the bias voltage at the substrate. These results indicate that the soft silicon substrate does not exert a significant effect on the results of measurements of the nanohardness of the films. The modulus of elasticity of the films proves to be more sensitive to the substrates, especially at high L.

Figure 13 shows the maximum values of H and E determined from the $H(L)$ and $E(L)$ dependences as functions of U_s. For the NbN films, the values of H tend to increase with increasing U_s. These values reach 29.5 GPa at $D \sim 50$ nm (Fig. 13a). In the case of the Nb–Si–N coatings, the maximum values of H = 31.6 GPa are attained at $U_s = -20$ V ($D \sim 47$ nm). A comparison of the results presented in Figs. 10 and 13 shows that the modulus of elasticity of the NbN and Nb–Si–N-films grows with increasing grain size.

It was established that the nanohardness is lower by approximately 10–20% in comparison with the Knoop hardness. Figure 14 shows the change in the

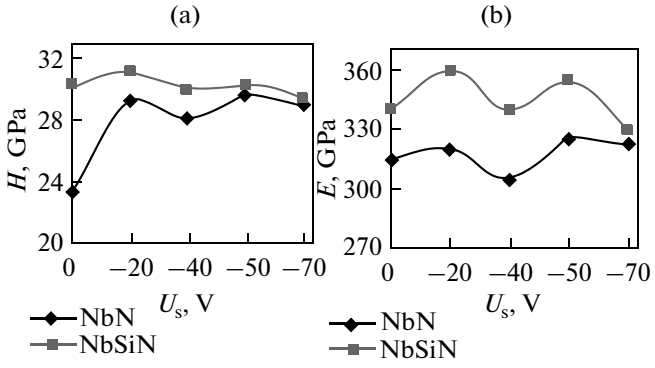

Fig. 13. Nanohardness (H) and the elasticity modulus (E) depending on the bias voltage at the substrate for NbN and Nb–Si–N coatings.

Knoop hardness H_K for NbN and Nb–Si–N coatings depending on the temperature of annealing (T_{ann}). The hardness increases a little after annealing at T_{ann} = 600°C and decreases with a further increase in T_{ann} to 1000°C. An increase in the hardness can be ascribed to a densification of the coatings because of crystalline reconstructions [21, 38–41]. A significant reduction in H_K at $T_{ann} > 600$°C can be connected with the oxidation, since the vacuum inside the chamber for the annealing was kept at a level of 0.001 Pa. This vacuum is insufficiently low to avoid oxidation at high T_{ann}. We can see from Fig. 14 that the number of clusters of Nb_2O_x and SiO_2 increases after the annealing of the Nb–Si–N film at 1000°C. The oxidation of Si_3N_4 and NbN can occur according to the following reactions [21, 35]:

$$Si_3N_4 + O_2 = 3SiO_2 + 2N_2,$$

$$2NbN + O_2 = Nb_2O_2 + N_2,$$

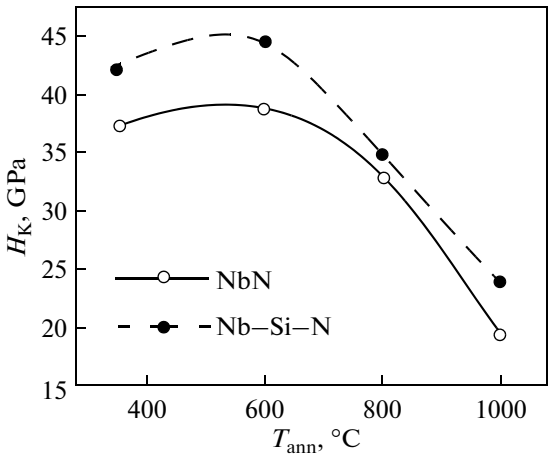

Fig. 14. Knoop hardness (H_K) of the NbN and Nb–Si–N films depending on the annealing temperature. Points at 350°C correspond to the conditions of the film deposition.

As a result, the concentration of oxygen grows and can reach 20 at %, as was shown by the EDX and XPS methods.

3.2. Theoretical Results

Figure 15 shows the atomic configurations for the δ-Si_3N_4(001) heterostructures. It can be seen that the optimization of the geometry of the initial heterostructure at 0 K preserved the heteroepitaxial structure, as is described for the TiN(001)/Si_3N_4 heterostructure in [28]. At 1400 K, the structure of the δ-Si_3N_4(001) interfaces changes. There are almost symmetrical shifts of the nitrogen atoms downward and upward in the layers located above and below the interfacial layer, as well as displacements of silicon atoms and breaksing of about half of Si–N bonds. This leads to the formation of distorted Si_3N_4-like blocks, which are represented by single SiN_4 and SiN_5 clusters. Along with the new Si_3N_4-like blocks, the original $B1$-type SiN_6 clusters [37] are present in the high-temperature heterostructure.

Since the length of the Si–N bond 1.75–1.77 Å in β-Si_3N_4 is considerably shorter than the length of the Nb–N bonds 2.205 Å in pure NbN, stresses appear in the NbN/Si_xN_y interfaces. These stresses and the tendency of silicon atoms to acquire a fourfold coordination with the atoms of nitrogen (as in Si_3N_4) are the basic factors that produce changes in the interface layers. The comparison of the structure and structural functions of the HT δ-Si_3N_4(001) interfaces with those of the amorphous Si_3N_4 calculated in [28] shows that the structure of the interface is very close to the structure of the over-coordinated amorphous Si_3N_4. Thus, the structure of the HT δ-Si_3N_4(001) interface is amorphous rather than heteroepitaxial, which agrees with our experiment.

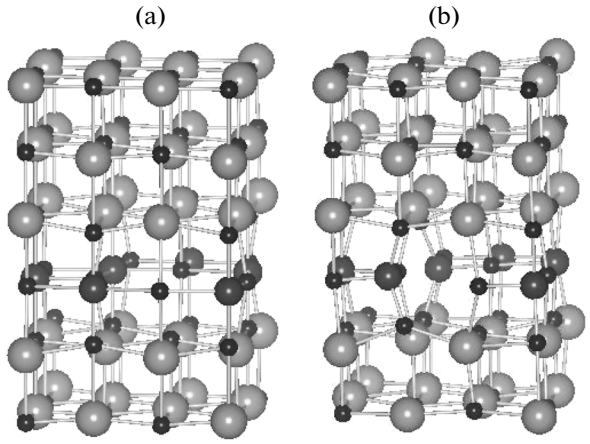

Fig. 15. Atomic configurations of the NbN(001)/$Si_{0.75}N$ heterostructures: (a) ZT in the equilibrium; and (b) HT in the equilibrium. Cutting of the bonds: 2.3 Å (Si–N) and 2.6 Å (Nb–N). Gray spheres designate Nb atoms; black large spheres, Si atoms; black small spheres, N atoms.

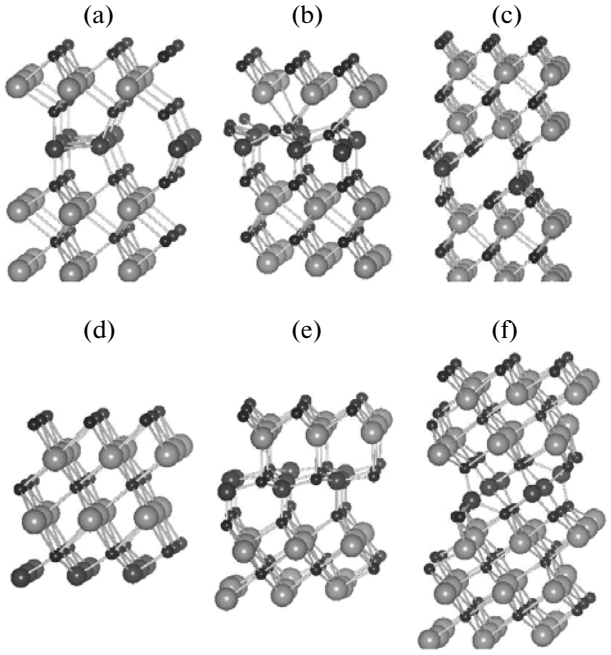

Fig. 16. Atomic configurations of HT heterostructures: (a) ε-SiN(001)); (b) ε-Si_3N_4–SiN(001); (c) ε-Si_3N_4–Si_2N_3(001); (d) δ-SiN(111); (e) δ-Si_3N_4–SiN(111); (f) δ-Si_3N_4–Si_2N_3(111). Cutting of the bonds: 2.3 Å (Si–N) and 2.6 Å (Nb–N). The designation of the atoms as in Fig. 15.

In Fig. 16, we show the high-temperature hexagonal heterostructures ε-NbN(001)/Si_xN_y and δ-NbN(111)/Si_xN_y. An analysis of the atomic configurations and total energies of the ZT and HT heterostructures (Table 2) shows that ε-SiN(001), ε-Si_3N_4–Si_2N_3(001), and δ-SiN(111) heterostructures only weakly change with the temperature. The initial heteroepitaxial layer in the ε-SiN(001) heterostructure changes already upon the static relaxation at 0 K. The interfaces in the ε-Si_3N_4-SiN(001) and δ-Si_3N_4–Si_2N_3(111) heterostructures become amorphous at a high temperature. As a result, the total energy of these systems increases with increasing temperature (Table 2).

Finally, an increase in the temperature favors the optimization of the δ-Si_3N_4–SiN(111) heterostructure and leads to a reduction in its total energy. Note that the fourfold coordination of silicon atoms in Si_3N_4–SiN and Si_3N_4–Si_2N_3 interfaces is retained also at a high temperature. It can be seen that the interface in the δ-SiN(111) heterostructure is heteroepitaxial and does not depend on temperature. These results show that only the HT ε-Si_3N_4–Si_2N_3(001), δ-SiN(111), and δ-Si_3N_4–SiN(111) interfaces are ordered of all possible configurations of interfaces examined here.

Figures 17 and 18 show the calculated tensile stress–strain curves for NbN and HT δ-Si_3N_4(001),

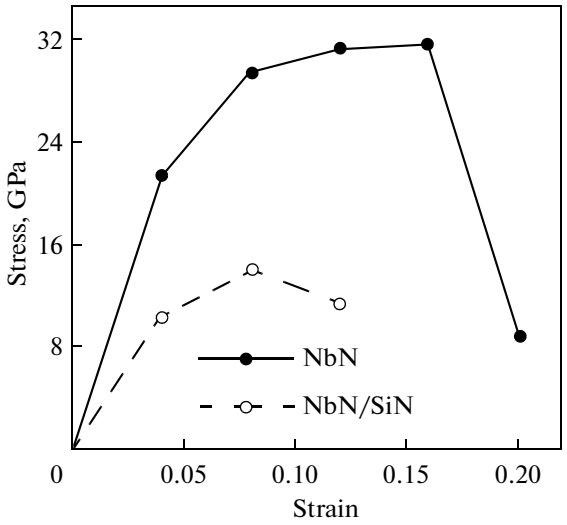

Fig. 17. Calculated tensile stress–strain curves along the [001] axis for the NbN and HT δ-Si_3N_4(001) heterostructures.

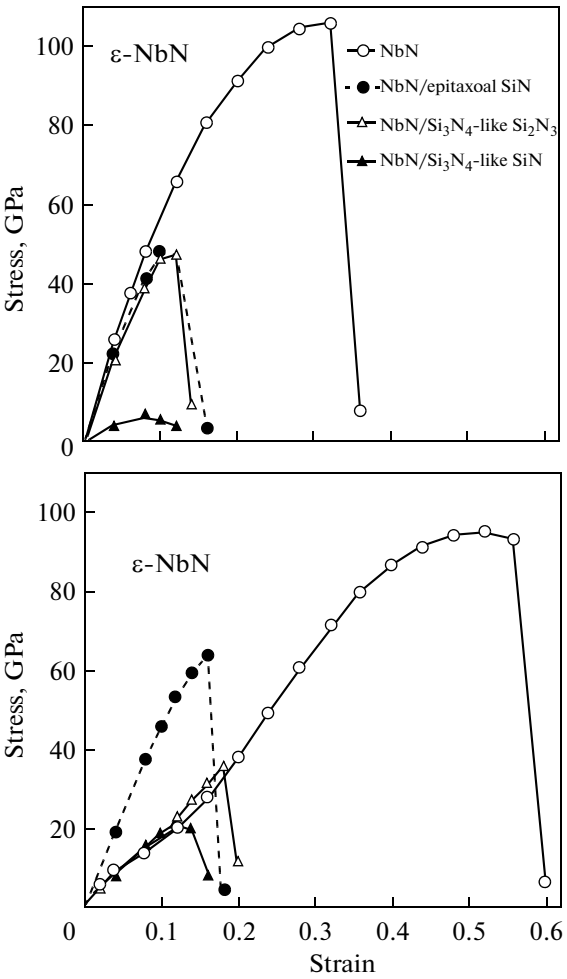

Fig. 18. Calculated tensile stress–strain curves along the [001] axis for (a) NbN and HT ε-NbN(001)/Si_xN_y and (b) δ-NbN(111)/Si_xN_y heterostructures.

ε-NbN(001)/Si_xN_y, and δ-NbN(111)/Si_xN_y heterostructures. The formation of interfaces in NbN leads to a decrease in the tensile strength. It can be seen that the least strength is characteristic of the δ-Si_3N_4(001) and ε-Si_3N_4–SiN(001) heterostructures.

It follows from these results that the formation of the interfacial layer of Si_xN_y in δ-NbN(001), δ-NbN(111), and ε-NbN(001) strongly destabilizes niobium nitride. The calculated δ-Si_3N_4-like interfaces have a structure close to amorphous, which is in agreement with the experiment [42–47]. The formation of interfaces does not lead to a strengthening of the chemical bond in heterostructures. Thus, the observed increase in the strength in the nanocomposite films based on NbN and Si_xN_y should be assigned mainly to the interfaces, which play the role of the barriers that impede the motion of dislocations. For the NbN/Si_xN_y heterostructures, in the absence of lattice defects (dislocations, point defects, etc.), our theoretical results predict a decrease in strength with the formation of Si_xN_y interfaces in NbN.

4. CONCLUSIONS

Nb–N and Nb–Si–N films on silicon plates have been obtained by magnetron sputtering using different bias voltages (U_s) at the substrate. Complex investigations of the properties and structure of the deposited films have been carried out. The studies using atomic-force microscopy (AFM) show that an increase in U_s and the introduction of silicon favor a reduction in the surface roughness. The XRD, XPS, and EDX analyses made it possible to establish the structure of the deposited films. The NbN and Nb–Si–N films had a nanocomposite structure. The Nb–Si–N films consist of clusters of δ-NbN_x nanocrystallites embedded into the amorphous SiN_x phase (nc-δ-NbN_x/a–Si_3N_4). The Nb–Si–N films possess a higher hardness ($H \sim 32$ GPa) in comparison with NbN films ($H \sim 29$ GPa) mainly due to the formation of a nanocomposite nc-δ-NbN_x/a–Si_3N_4 structure. The nanohardness and the modulus of elasticity of the Nb–Si–N-films weakly depend on the bias voltage at the substrate. It is assumed that some increase in the nanohardness of nanocomposite films in comparison with that of NbN films is caused by the greater sizes of grains of δ-NbN_x in the Nb–Si–N films (7–50 nm). The Knoop hardness decreases with an increase in the temperature of annealing from 600 to 800 and 1000°C because of the partial oxidation of NbN and Si_3N_4.

The results of first-principles calculations of NbN/Si_xN_y heterostructures show that, in the absence of lattice defects, the formation of Si_xN_y interface should not lead to a strengthening of the chemical bonds and increasing of the ideal tensile strength of the nanocomposites. Therefore, the observed increase in the strength of the nanocomposite nc-δ-NbN/a–Si_3N_4 coatings should be assigned mainly to the interfaces, which play the role of barriers that impede the movement of dislocation.

REFERENCES

1. S. Veprek, "Recent attempts to design new super- and ultrahard solids leads to nano-sized and nano-structured materials and coatings," J. Nanosci. Nanotech. **11**, 14–35 (2011).
2. R. A. Andrievsky, I. A. Anisimova, and V. P. Anisimov, "Structure and microhardness of TiN compositional and alloyed films," Thin Solid Films **205**, 171–175 (1991).
3. P. J. Martin and A. Bendavid, "The filtered arc process and materials deposition," Surf. Coat. Technol. **142–144**, 7–10 (2001).
4. A. Bendavid, P. J. Martin, T. J. Kinder, and E. W. Preston, "The deposition of NbN and NbC thin films by filtered vacuum cathodic arc deposition," Surf. Coat. Technol. **163–164**, 347–352 (2003).
5. V. N. Zhitomirsky, I. Grimberg, L. Rapoport, N. A. Travitzky, R. L. Boxman, S. Goldsmith, A. Raihel, I. Lapsker, and B. Z. Weiss, "Structure and mechanical properties of vacuum arc-deposited NbN coatings," Thin Solid Films **326**, 134–142 (1998).
6. R. L. Boxman, V. N. Zhytomirsky, I. Grimberg, L. Rapoport, S. Goldsmith, and B. Z. Weiss, "Structure and hardness of vacuum arc deposited multi-component nitride coatings of Ti, Zr and Nb," Surf. Coat. Technol. **125**, 257–262 (2000).
7. V. N. Zhitomirsky, "Structure and properties of cathodic vacuum arc deposited NbN and NbN-based multi-component and multi-layer coatings," Surf. Coat. Technol. **201**, 6122–6130 (2007).
8. M. Benkahoul, E. Martinez, A. Karimi, R. Sanjines, and F. Levy, "Structural and mechanical properties of sputtered cubic and hexagonal NbN_x thin films," Surf. Coat. Technol. **180–181**, 178–183 (2004).
9. G. A. Fontalvo, V. Terziyska, and C. Mitterer, "High-temperature tribological behavior of sputtered NbN_x thin films," Surf. Coat. Technol. **202**, 1017–1022 (2007).
10. M. Wen, C. Q. Hu, C. Wang, T. An, Y. D. Su, Q. N. Meng, and W. T. Zheng, "Effects of substrate bias on the preferred orientation, phase transition and mechanical properties for NbN films grown by direct current reactive magnetron sputtering," J. Appl. Phys. **104**, 023527–023527 (2008).
11. J. E. Alfonso, J. Buitrago, J. Torres, J. F. Marco, and B. Santos, "Influence of fabrication parameters on crystallization, microstructure, and surface composition of NbN thin films deposited by rf magnetron sputtering," J. Mater. Sci. **45**, 5528–5533 (2010).
12. K. Singh, A. C. Bidaye, and A. K. Suri, "Magnetron sputtered NbN films with Nb interlayer on mild steel," Int. J. Corrosion **2011**, 748168 (2011).
13. N. Hayashi, I. H. Murzin, I. Sakamoto, and M. Ohkubo, "Single-crystal niobium nitride thin films

prepared with radical beam assisted deposition," Thin Solid Films **259**, 146–149 (1995).

14. G. Cappuccio, U. Gambardella, A. Morone, S. Orlando, and G. P. Parisi, "Pulsed laser ablation of NbN/MgO/NbN multilayers," Appl. Surf. Sci. **109–110**, 399–402 (1997).
15. Y. Dong, Y. Liu, J. Dai, and G. Li, "Superhard Nb–Si–N composite films synthesized by reactive magnetron sputtering," Appl. Surf. Sci. **252**, 5215–5219 (2006).
16. M. Benkahoul, C. S. Sandu, N. Tabet, M. Parlinska-Wojtana, A. Karimia, and F. Levy, "Effect of Si incorporation on the properties of niobium nitride films deposited by dc reactive magnetron sputtering," Surf. Coat. Technol. **188–189**, 435–439 (2004).
17. C. S. Sandu, M. Benkahoul, R. Sanjines, and F. Levy, "Model for the evolution of Nb–Si–N thin films as a function of Si content relating the nanostructure to electrical and mechanical properties," Surf. Coat. Technol. **201**, 2897–2903 (2006).
18. C. S. Sandu, R. Sanjines, M. Benkahoul, F. Medjani, and F. Levy, "Formation of composite ternary nitride thin films by magnetron sputtering codeposition," Surf. Coat. Technol. **201**, 4083–4089 (2006).
19. J. Wang, Z. Song, and K. Xu, "Influence of sputtering bias on the microstructure and properties of Nb–Si–N films," Surf. Coat. Technol. **201**, 4931–4934 (2007).
20. Z. X. Song, Y. Wang, C. J. F. Wang, C. L. Liu, and K. W. Xu, "The effect of N_2 partial pressure on the properties of Nb–Si–N films by RF reactive magnetron sputtering," Surf. Coat. Technol. **201**, 5412–5415 (2007).
21. J. J. Jeong and C. M. Lee, "Effects of post-deposition annealing on the mechanical and chemical properties of the Si_3N_4/NbN multilayer coatings," Appl. Surf. Sci. **214**, 11–19 (2003).
22. J. J. Jeong, S. K. Hwang, and C. Lee, "Hardness and adhesion properties of HfN/Si_3N_4 and NbN/Si_3N_4 multilayer coatings," Mater. Chem. Phys. **77**, 27–33 (2003).
23. W. Wen, Q. N. Meng, C. Q. Hu, T. Ana, Y. D. Sua, W. X. Yua, and W. T. Zheng, "Structure and mechanical properties of δ-NbN/SiN_x and δ'-NbN/SiN_x nanomultilayer films deposited by reactive magnetron sputtering," Surf. Coat. Technol. **203**, 1702–1708 (2009).
24. S. Baroni, CorsoA. Dal, S. de Gironcoli, P. Giannozzi, C. Cavazzoni, G. Ballabio, S. Scandolo, G. Chiarotti, P. Focher, A. Pasquarello, K. Laasonen, A. Trave, R. Car, N. Marzari, and A. Kokalj, http://www.pwscf.org/
25. J. P. Perdew, K. Burke, and M. Ernzerhof, "Generalized gradient approximation made simple," Phys. Rev. Lett. **77**, 3865–3868 (1996).
26. D. Vanderbilt, "Soft self-consistent pseudopotentials in a generalized eigenvalue formalism," Phys. Rev. B: Condens. Matter **41**, 7892–7895 (1990).
27. S. R. Billeter, A. Curioni, and W. Andreoni, "Efficient linear scaling geometry optimization and transition-state search for direct wavefunction optimization schemes in density functional theory using a plane-wave basis," Comput. Mater. Sci. **27**, 437–445 (2003).
28. V. I. Ivashchenko, S. Veprek, P. E. A. Turchi, and V. I. Shevchenko, "Comparative first-principles study of TiN/SiN_x/TiN interfaces," Phys. Rev. B: Condens. Matter Mater. Phys. **85**, 195403 (2012).
29. S. Wang, R. Gudipati, A. S. Rao, T. J. Bostelmann, and Y. G. Shen, "First-principles calculations for the elastic properties of nanostructured superhard TiN/Si_xN_y superlattices," Appl. Phys. Lett. **91**, 081916 (2007).
30. H. J. Monkhorst and J. D. Pack, "Special points for Brillouin-zone integrations," Phys. Rev. B: Solid State **13**, 5188–5192 (1976).
31. E. I. Isaev, S. I. Simak, I. A. Abrikosov, R. Ahuja, Yu. Kh. Vekilov, M. I. Katsnelson, A. I. Lichtenstein, and B. Johansson, "Phonon related properties of transition metals, their carbides, and nitrides: A first-principles study," J. Appl. Phys. **101**, 123519–18 (2007).
32. X-ray powder diffraction file [089-5007].
33. A. Darlinski and J. Halbritter, "On the identification of interface oxides and interface serration by ARXPS," Z. Fresenius Annal. Chem. **329**, 266–271 (1987).
34. G. Beamson and D. Briggs, *High Resolution XPS of Organic Polymers* (The Scienta ESCA300 Data-Base. Wiley Interscience. 1992).
35. G. Jouve, C. Severac, and S. Cantacuzene, "XPS study of NbN and (NbTi)N superconducting coatings," Thin Solid Films **287**, 146–153 (1996).
36. A. N. Christensen, O. W. Dietrich, W. Kress, W. D. Teuchert, and R. Currat, "Phonon anomalies in transition metal nitrides: δ-NbN," Solid State Commun. **31**, 795–799 (1979).
37. V. I. Ivashchenko, P. E. A. Turchi, and E. I. Olifan, "Phase stability and mechanical properties of niobium nitrides," Phys. Rev. B: Condens. Matter Mater. Phys. **82**, 054109 (2010).
38. A. D. Pogrebnjak, A. P. Shpak, N. A. Azarenkov, and V. M. Beresnev, "Structures and properties of hard and superhard nanocomposite coatings," Phys.–Usp. **52**, 29–54 (2009).
39. A. D. Pogrebnjak, O. V. Sobol, V. M. Beresnev, P. V. Turbin, G. V. Kirik, N. A. Makhmudov, M. V. Il'yashenko, A. P. Shypylenko, M. V. Kaverin, M. Yu. Tashmetov, and A. V. Pshyk, "Phase composition, thermal stability, physical and mechanical properties of superhard on base Zr–Ti–Si–N nanocomposite coatings," Nanocomp. Coat. Nanostruct. Mater. Nanotechnol. IV: Ceram. Eng. Sci. Proceed **31** (7), 127–138 (2010).
40. A. D. Pogrebnjak, "Structure and properties of nanostructured (Ti–Hf–Zr–V–Nb)N Coatings," J. Nanomater. **2013**, Art. ID 780125 (2013).
41. A. D. Pogrebnjak, A. P. Shpak, V. M. Beresnev, D. A. Kolesnikov, Yu. A. Kunitskii, O. V. Sobol, V. V. Uglov, F. F. Komarov, A. P. Shypylenko, N. A. Makhmudov, A. A. Demyanenko, V. S. Baidak, and V. V. Grudnitskii, "Effect of thermal annealing in vacuum and in air on nanograin sizes in hard and superhard coatings Zr–Ti–Si–N," J. Nanosci. Nanotech. **12**, 9213–9219 (2012).

42. J. Musil, "Hard nanocomposite coatings: Thermal stability, oxidation resistance and toughness," Surf. Coat. Tech. **207**, 50–65 (2012).

43. S. Veprek and M. G. J. Veprek-Heijman, "Limits to the preparation of superhard nanocomposites: Impurities, deposition and annealing temperature," Thin Solid Films **522**, 274–282 (2012).

44. A. D. Pogrebnjak, A. G. Ponomarev, A. P. Shpak, and Yu. A. Kunitskii, "Application of micro- and nanoprobes to the analysis of small-sized 3D materials, nanosystems, and nanoobjects," Phys.–Usp. **55**, 270–300 (2012).

45. V. Ivaschenko, S. Veprek, A. Pogrebnjak, and B. Postolnyi, "First–principles quantum molecular dynamics study of $Ti_xZr_{1-x}N(111)/SiN_y$ heterostructures and comparison with experimental results," Sci. Tech. Advan. Mater. **15**, 025007 (2014).

46. A. D. Pogrebnjak, S. N. Bratushka, V. M. Beresnev, and N. Levintant-Zayonts, "Shape memory effect and superelasticity of titanium nickelide alloys implanted with high ion doses," Rus. Chem. Rev. **82**, 1135–1168 (2013).

47. A. D. Pogrebnjak and V. M. Beresnev, *Nanocoatings, Nanosystems, Nanotechnologies* (Bentham Sci. Publ., New York, 2012).

Translated by S. Gorin